



Supplementary Materials for
Reversible oxygen migration and phase transitions in hafnia-based ferroelectric devices

Pavan Nukala*, Majid Ahmadi, Yingfen Wei, Sytze de Graaf, Evgenios Stylianidis, Tuhin Chakraborty, Sylvia Matzen, Henny W. Zandbergen, Alexander Björling, Dan Mannix, Dina Carbone, Bart Kooi, Beatriz Noheda*

*Corresponding author. Email: pnukala@iisc.ac.in (P.N.); b.noheda@rug.nl (B.N.)

Published 15 April 2021 on *Science* First Release
DOI: 10.1126/science.abf3789

This PDF file includes:

Materials and Methods
Supplementary Text
Figs. S1 to S11
References

Materials and Methods

Synthesis by Pulsed Laser Deposition: LSMO (30 nm)/HZO (6 nm)/LSMO (30 nm) layers were grown epitaxially on Nb:STO via pulsed laser deposition (PLD). The growth conditions are described elsewhere (7). Pt (200 nm) was sputtered on the top-electrode (LSMO).

***In situ* STEM set-up, imaging and biasing techniques:** The set-up of the holder, biasing system in Thermo Fisher Scientific Themis Z (monochromated and double corrected) microscope is shown in Fig. S1A. In-situ biasing cum heating customized double tilt holder (HennyZ, Fig. S1B) was used to host the cross-sectional devices (zone axis: [110] Nb:STO) prepared on a MEMS based SiN_x chip (Fig. S1C,D preparation procedure described in the next section). Biasing was performed through Keithley 4200 parameter analyzer by using two SMUs (source measuring units, Fig S1A). Atomic resolution imaging (while biasing) was performed at 300 kV through HAADF-STEM, and more importantly integrated differential phase contrast (iDPC) STEM to image low Z elements such as oxygen. Beam convergence angle was 22.4 mrad. Data from segmented detectors were acquired under the collection angles from 6-23 mrad. H(M)AADF-STEM images were simultaneously acquired with collection angles > 23 mrad. Energy dispersive spectroscopy (EDS) was performed using two large area detectors in total capturing 1.76 steradian. Spectra were acquired from various regions in the capacitor structure at a combined signal of 10-15 kcps for over 1 hour. Voltage is always applied to the top electrode, with bottom electrode at 0 V (Fig S1E).

***In situ* biasing device fabrication:** MEMS based micro heater & electrical biasing chip (developed by HennyZ, see Fig. S1C-E) is used for hosting the TEM cross-sectional lamella, and connecting the lamella to the external pads. This chip has 6 electrodes, 3 on each side of the SiN_x membrane. The outermost electrodes are connected to the microheater and can heat the TEM lamella very locally up to 1000 °C. The innermost Pt-electrodes are used for biasing. A focused ion beam (FIB, FEI Helios G4 CX) based sample preparation protocol was developed in-house for *in situ* biasing experiments. Electron transparent regions were created in the region between the inner most electrodes of interest on the SiN_x membrane by drilling a hole using the Ga ion beam. Cross-sectional chunks (dimensions: 10 x 1.5 x 5 μm³) were initially thinned down to 300-500 nm thickness using standard focus ion beam (FIB) based processing at 30 kV, and then transferred onto the SiN_x membrane of the chip (Fig. S1E). The top (Pt) and bottom electrode (substrate) were then connected to the electrodes on the chip through e-beam induced Pt deposition (EBID). Certain windows (~1 x 3 μm²) on the lamella were thinned down to ~50 nm using the Ga ion beam at 16

kV accelerating voltage, and finally several low kV cleaning steps (5 and 2 kV) were used not only to clean the side surfaces of the lamella, but also to remove the excess Pt deposition (Fig S1E). Electrical measurements were performed *ex situ* after every step to understand any possible leakage sources, and further milling and cleaning steps were performed to remove these sources.

Regular device fabrication: Tunnel junction devices (Co/HZO (2 nm)/LSMO) were fabricated using the procedure described in ref. 44. Two types of ferroelectric capacitors were fabricated: TiN/HZO (7 nm)/LSMO (30 nm)//STO devices were made by depositing TiN as the top electrodes using standard photolithography and sputter deposition followed by lift-off procedure on the rest of the stack grown by PLD. LSMO/HZO/LSMO capacitors were also fabricated. The entire stack was first grown using PLD. Then devices were lithographically defined by etching the top LSMO, HZO and 6 nm of bottom LSMO layer away from the regions of interest using Ar ion-beam etching. Cross sections from these devices were made through standard FIB based TEM cross-sectional lamella preparation procedure.

The tunnel junction devices were tested *ex situ* with +6/-6 V sub-millisecond rectangular pulses for 100s of cycles. Cross-section TEM lamellae were made from one sample in the high resistance state, and another one in the low resistance state. The TiN/HZO/LSMO capacitors were tested for ferroelectric switching using the PUND scheme at +/- 5.5 V using triangular pulses of rise and fall time of 250 μ s for tens of cycles. Results presented in Fig. 4C-E are from a cross-sectional lamella of such capacitor, which was eventually ferroelectrically switched “down” with a +5.5 V pulse (Fig. S8).

Operando x-ray diffraction:

Au/HZO (6 nm)/LSMO and LSMO/HZO (6 nm)/LSMO capacitors were fabricated using a lithography based process (Fig S9), and tested using *operando* synchrotron X-Ray diffraction at the NanoMAX beam line of the MAX IV synchrotron (50,51), using a nanobeam with 400 nm x 100 nm footprint. Both devices were cycled at 100 Hz in a modest voltage range between -3.5 and 3.5 V for tens of thousands of cycles (Fig S10). The HZO (111) Bragg peak was measured with a 2D pixel detector before and after electrical cycling to observe the impact of the voltage change onto the crystal structure of the device.

Energy dispersive spectroscopy quantification:

EDS spectra of LSMO recorded with the Themis Z electron microscope were quantified after background subtraction using the Brown-Powell model (52). Oxygen atomic percentages in Fig.

1G were determined from 20 x 5 nm² regions with one on the top electrode, and three in the bottom electrode with varying distance to the HZO as marked L0, L1 and L2 in Fig. 1F.

\ddot{V}_o displacement analysis in HZO layer:

The cationic lattice of the supercell was first constructed by identifying the cation positions through a peak finding algorithm after assigning a finite width defined by a mask around each peak. The rest of the lattice in the supercell is the anionic lattice (see Fig. S4). We quantify the \ddot{V}_o migration as a function of bias in this supercell by estimating the difference between the centers of mass (CoM) of the cations and anions. Under the assumption that cations do not move at small voltages, we can relate this quantity directly to the migration of \ddot{V}_o . The choice of the mask defining the size of the cations, and the pixel size determine the errors in estimation of the displacement, although peak fitting can occur with sub-pixel size precision.

P-V hysteresis measurements:

P-V loops were measured using a dynamic hysteresis measurement scheme on TiN/HZO/LSMO//STO capacitors. A triangular voltage waveform of 1 kHz from 0 to 5 to -5 to 0 V (defining one period) were applied to the device at various temperatures, and corresponding currents were measured. Polarization was calculated using the formula $P = \frac{1}{A} \int i dt$, where A is the device cross-sectional area, i is the measured current, and t is the time.

Supplementary Text

S1. The LSMO layer in the as-deposited film is oriented with $[001]_{\text{pseudocubic}}$ (c-axis) out of plane, and observed along the $[110]_{\text{pseudocubic}}$ (pc) (zone axis). Schematics of A-site (La/Sr), B-site (Mn) and oxygen column arrangements are shown in Fig. 1A. The $a\bar{a}a$ octahedral tilts typical of rhombohedral LSMO reveal themselves as antiphase δ tilts in this zone (alternating positive and negative Mn-O-Mn bond angles)(35). Deviations of Mn columns from octahedral coordination in the virgin state, although present are very minimal, and can be considered to be disorder induced perturbations of the standard structure. Even some disorder in the octahedral tilt angles (165-176°) can be seen in Figs 1A and S2A.

S2: Square pyramidal coordination is typical of the BM phases of strontium manganite (SMO, SrMnO_{2.5}, Fig. S2D). When BM-SMO is viewed along $[110]_{\text{pc}}$ zone axis, it shows two important features (i) Mn displacements away from the octahedral coordination along $[1-10]_{\text{pc}}$ and (ii) a resolvable doubling of alternate oxygen columns between Mn columns with ~90 pm projected

distance between the columns along $[1-10]_{pc}$ (horizontal direction in Fig.1B, Fig. S2B,D). Both these features, characteristic of square pyramidal coordination are present in the BM precursor phase of LSMO (Fig S2C, Mn displacement marked in green arrows, Oxygen column separation marked by blue arrows), albeit in randomly varying directions (not just along $[1-10]$). The reported changes in structure at 2 V (Fig. 1B) are hysteretic and remain upon removing the external bias.

In the following we present the Mn displacements and corresponding histograms for both the device in virgin state, as well as several regions for the device biased at 2V. Mn positions and O positions were computed as the centroid of the Mn and O atomic column intensity distributions, respectively. Displacement of Mn from the center of the oxygen octahedron was calculated as the difference between the position of Mn and the center of mass of O-O bond on either side of the Mn. Angle of the displacement is measured with respect to the in-plane direction (horizontal). Arrow plots are shown in Fig. S3A,B, to visualize the displacements directly on the images.

Fig. S3A shows the displacement vectors of a representative region in the virgin state, where we measured no significant Mn displacement (<5 pm, which is within the sensitivity of the measurement). This is consistent with our diagnosis of virgin state as consisting mostly of regular MnO_6 octahedra (non-distorted).

Fig. S3B shows two representative regions biased at 2 V. Here, we indeed see random displacements of Mn atoms (with displacement magnitudes as large as 50 pm). These analyses were carried out on 6 different regions of interest across various images. The polar scatter plot of Mn displacements (on circles of radius 60 pm) comparing the virgin state (from 60 Mn columns) and the biased state (from 329 Mn columns) is shown in Fig. S3C. While in virgin state there are almost no displacements, in the biased state the displacements vary from 0 to 55 pm (mean value :18.6 pm, std. deviation:10.2 pm) with random angular dispersion. These displacements result in a distortion of an octahedron into square pyramids, a prominent feature of the BM-precursor phase, further validating our previous claims on the structure of this phase.

S3: In the BM phase shown in Fig. 1C (viewed along a-axis), the perovskite-like layer consists of MnO_6 octahedra, whereas the oxygen deficient Mn-O layer consists of MnO_4 tetrahedra, which along the $[1-10]$ direction, alternate between pointing towards each other and away from each other. Also observable is another domain viewed along c-axis (Fig. S3A), where Mn columns in the oxygen deficient Mn-O layer appear more symmetrically arranged. In Fig. S3B, a region is shown with the field of view of both the BM domains.

S4: Oxygen vacancies are known to cause some lattice expansion even in virgin samples. These vacancies are typically a result of not just the growth conditions of the film, but also the fact that LSMO grows under tensile strain on STO and Nb:STO (which promotes oxygen vacancies). See ref 6.

S5: We classify the effects that we observe in various experiments as short-term and accumulated short-term and long-term effects. For clarity we define our various experiments as follows:

- a) Short term effects: (a) 100-few kHz switching, <10 cycles, <6 V (Fig 4D,E) ; (b) 100-few kHz switching, tens of thousands of cycles at <3.5 V (operando synchrotron cycling experiments)
- b) Accumulated short term effects: 100-few kHz switching, hundreds of cycles @ 6 V (tunnel junctions, Fig 4A,B, Fig. S7)
- c) Long term effects: DC stressing (in-situ TEM experiments, and operando XRD DC biasing experiments)

It may be seen that voltage time dilemma is taken into consideration in defining these effects. For e.g. hundreds of cycles @ 6V still shows a more accumulated short-term effect, than tens of thousands of cycles @ 3.5 V.

S6: The saturation polarization (P_s) of the unit cell (as shown in Fig. S5C) is estimated in 2 different ways.

- (i) Through a peak-fitting algorithm the anionic positions (y_i) and cationic positions (x_i) were obtained in a unit cell. Then $P_r = \sum(4x_i - 2y_i)/V$, where V is the Volume of the unit cell (4 and -2 are the Born effective charges of Hf/Zr and oxygen respectively). The unit cell was chosen such that $P_r = 0$ in the symmetrized paraelectric phase (ref. 7). This yielded $P_r < 2 \mu\text{C}/\text{cm}^2$ (displacement < 10 pm) for HZO across 14 different unit cells in the $R3m$ phase. This procedure assumes HZO is completely stoichiometric, and P_r was similarly estimated on the $R3$ phase in ref 40. Note that for similar samples in $R3m$ phase, $P_r = 35 \mu\text{C}/\text{cm}^2$ was measured through macroscopic electrical switching experiments.
- (ii) With the new information from this work on the oxygen deficiency of the $R3m$ HZO phase, the stoichiometric assumption presented in (i) does not hold. So, we calculated the P_r by estimating the center of mass of the cationic lattice and the non-cationic part (anionic lattice) in every unit cell (Fig. S5C). The difference in the center of masses

gives a displacement of $\sim 38 (\pm 8)$ pm in the unit cell shown in Fig. S5C (from the domain on the left in Fig. 3E in the manuscript). This suggests that \ddot{V}_o is responsible for almost 4 times increase in the displacement (compared to the stoichiometric lattice in (i)). Whether this will cause significant improvement in direct estimation of P_r cannot be established without the knowledge on the Born charges of cations and anions in this oxygen deficient HZO lattice. Upon assuming that the cationic born charges in this configuration still remains +4, we estimate $P_r < 9 \mu\text{C}/\text{cm}^2$. In any case, there exists a clear mismatch with the value obtained from electrical measurements, strongly supporting that most of the switching arises from oxygen voltammetry process.

S7: The increase of remnant polarization (P_r) with temperature presented in Fig. 4C (see also Fig. S6) is consistent with the fact that \ddot{V}_o migration kinetics improves with temperature, clarifying that polarization switching and \ddot{V}_o are intertwined mechanisms. In conventional ferroelectrics, P_r is expected to degrade with increasing temperature owing to increased thermal fluctuations. Note that similar unconventional behavior was measured by Fengler and coworkers from 25°C to 125°C on ALD deposited HZO samples with TiN electrodes in ref 53.

Another interesting observation from these measurements is the pronounced presence of imprint (internal field) at low temperatures, which decreases towards zero at room temperature. This can be rationalized as a result of increased sluggishness of the oxygen diffusion during the topotactic phase transitions that follow oxygen migration (discharge mechanism) at low temperatures, resulting in accumulation of charged vacancies and thus space charge (32). However, detailed modeling of this interesting aspect belongs to the gamut of further work.

S8: To address the question of what will happen if one of the electrodes cannot be a sink or source of oxygen, we present results of *operando* X-ray diffraction measurements from Au/HZO/LSMO devices and compare them with LSMO/HZO/LSMO devices. Upon cycling, Au/HZO/LSMO capacitors show FE switching peak on the positive bias side, and different leakage/field-assisted tunneling characteristics for the up and down polarized state on the negative bias side (Fig. S10A). We have measured the (111) Bragg peak of HZO with a 2D detector in a fixed position (Fig. S10B) before, during and after cycling. This peak contains a bright specular part (with specular contributions from all the interfaces of the heterostructure in addition to the Bragg peak of HZO),

and a diffuse off-specular part (only arising from HZO). By masking the specular part, and projecting and interpolating the detector image onto the 2θ axis (2θ projection), we can analyse the changes in the (111) lattice parameter of HZO upon biasing. The cycling was performed at 100 Hz between -3.5 and 3.5 V (Fig. S10C) for tens of thousands of times. Note that this is a modest cycling at low voltages and effects of fatigue need not to be considered. Thus this is still short-term ferroelectricity, as defined in S5.

Measurements on the virgin samples in both types of capacitors are consistent with the growth of rhombohedral HZO along the [111] direction, with a Bragg peak position at $2\theta=26.5^\circ$ or $d_{(111)}=2.98$ Å (Fig. S10D,E). For the LSMO/HZO/LSMO devices, diffraction measurements of the cycled state do not show any significant difference (Fig. S10D). However, in the case of Au/HZO/LSMO, we see that a peak appears at $2\theta=24.9^\circ$ upon cycling, consistent with the presence of the monoclinic phase of HZO, that coexists with the r-phase (Fig. S10E,F). This confirms that the HZO layer itself is forced to act as source/sink of oxygen vacancies when Au is used as a top electrode, resulting in a reversible phase transitions even with low voltage pulses and modest cycling. In other words, even for short term ferroelectric switching, the HZO layer in Au/HZO/LSMO devices acts as a sink and a source of oxygen vacancies (and not just a conduit), and this results in phase transitions even in HZO.

Finally, we also followed the changes in the lattice parameters of HZO by applying DC bias from 0 to 3.5 V after cycling. We observe that the contribution from the monoclinic phase increases steadily with increasing positive bias (Fig. S11), which is the same long term effect seen in the LSMO/HZO/LSMO capacitors using in situ TEM measurements.

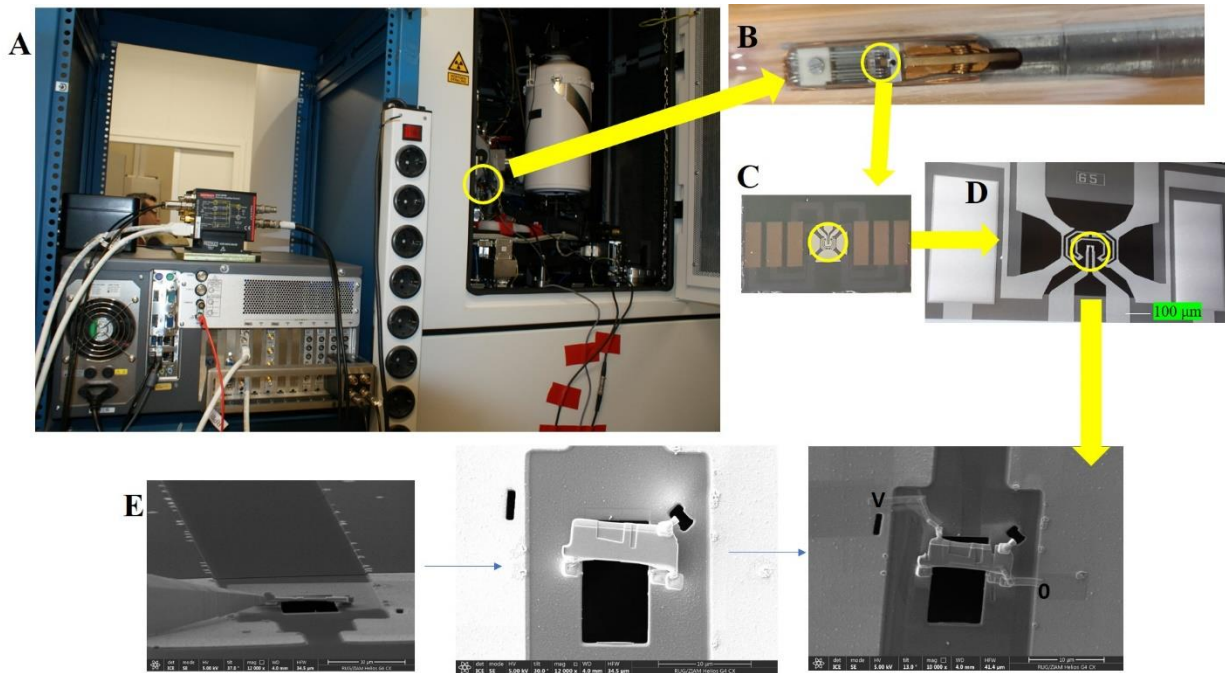
S9: Our thesis is that oxygen vacancy migration is very much intertwined with polarization switching, and that these are not independent from each other. It has been repeatedly reported that in hafnia-based ferroelectrics (unlike in conventional ferroelectrics), P_r increases as the film thickness decreases. This is very much consistent with our thesis. We remain agnostic about how exactly the oxygen migration couples to polarization switching and deem this to be a problem for the future.

S10: Another implication of the present work is the estimation of the field drop across the insulator in Metal-Insulator-Metal stacks. With an oxygen conducting memristor such as LSMO as one of

the metals, (e.g. Metal-HZO-LSMO) stacks, field drops (in context of coercive field estimations) across the insulator are typically overestimated due to not considering the field drop in the LSMO layer when oxygen begins to migrate. Thus, in this work we do not mention the fields, rather just report the values of voltages during electrical biasing.

Supplementary Figures

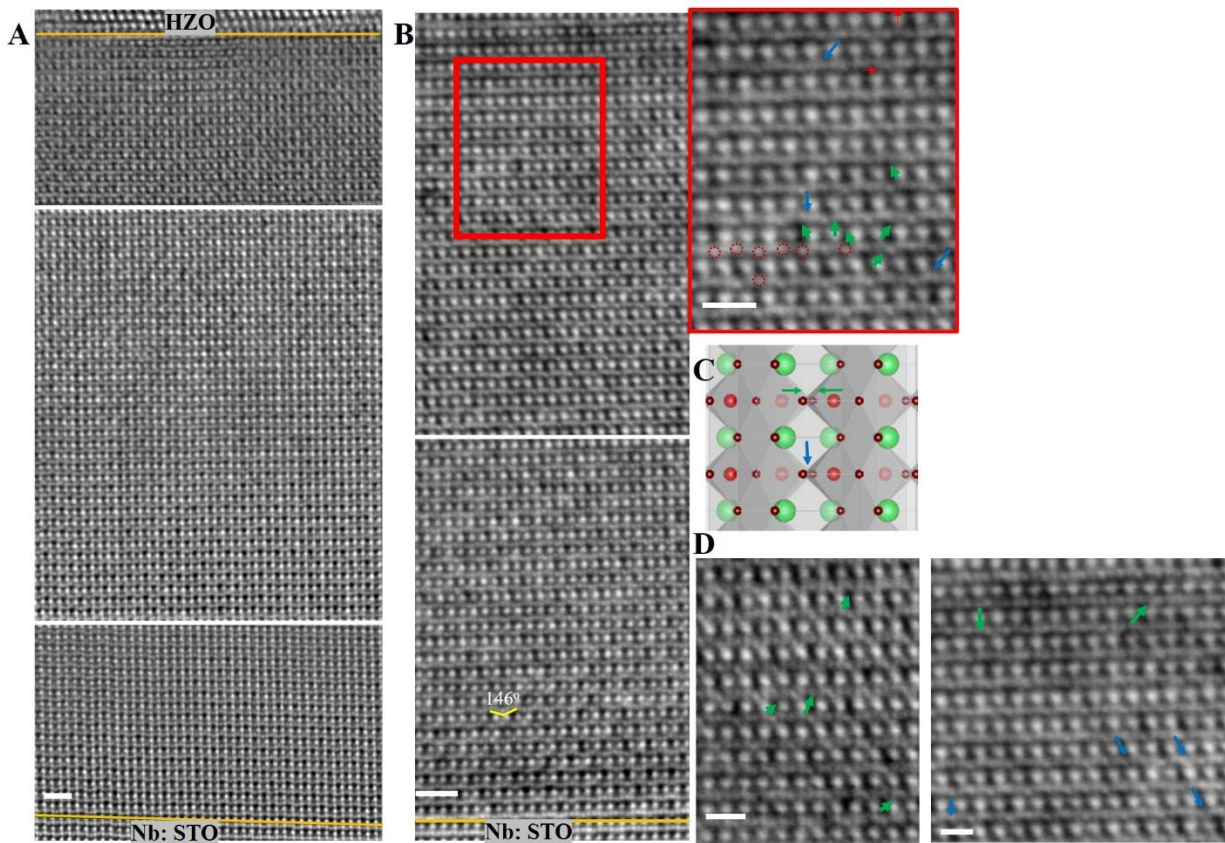
Fig. S1



In-situ biasing set-up and sample preparation

(A) Set-up showing Keithley 4200 parameter analyzer with two SMUs connected through a switch box (PMU) to the two leads of an in-situ biasing holder, inserted inside the electron beam column. (B) Optical photo of the biasing/heating holder with the inner two leads for biasing, and outer four to resistively heat the MEMS chip, shown in (C). (D) SEM image of the SiN_x (300 nm) membrane hosting the micro-heater, as well as biasing electrodes (inner most). (E) FIB based lamella transfer procedure onto the SiN_x membrane with electron transparent hole created *a-priori* (protocol described in materials and methods).

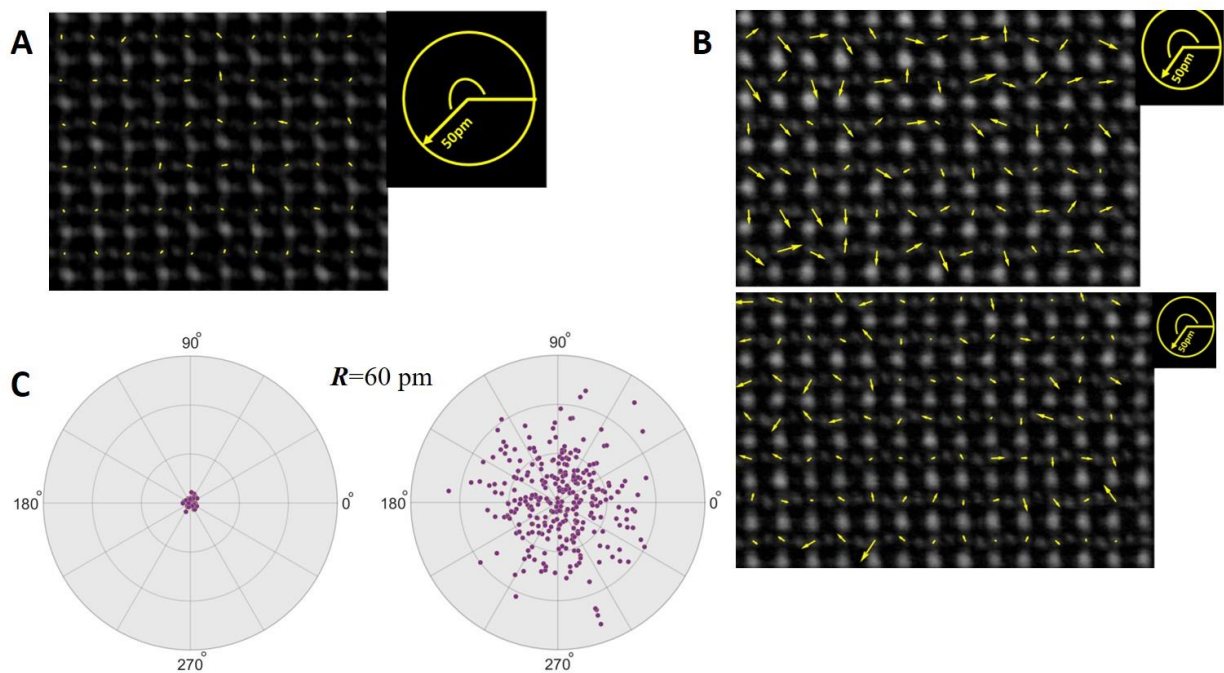
Fig. S2



Understanding the structural features of perovskite and BM-precursor phases

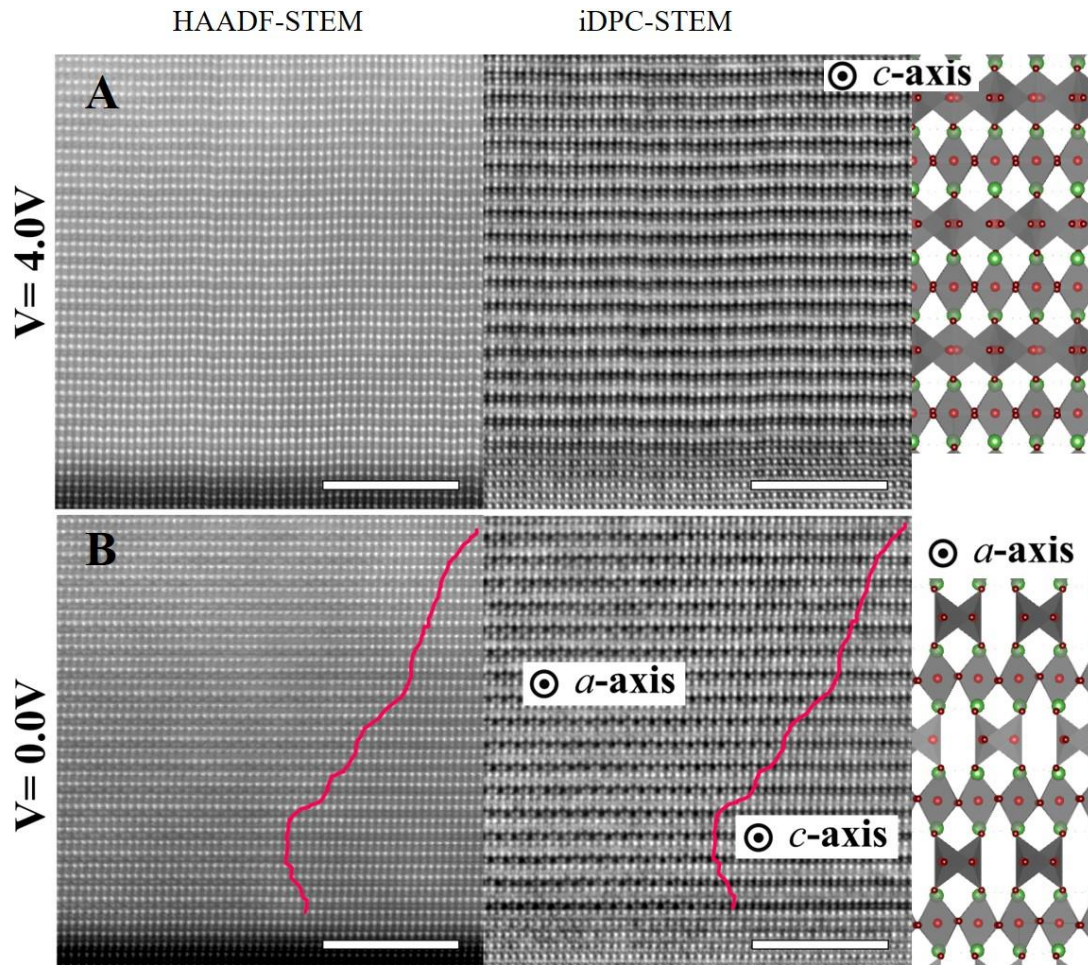
(A) Overview iDPC-STEM stitched images in the virgin state. (B) Overview iDPC-STEM stitched images at 2 V. Region enclosed in the red box is zoomed in the inset. Exaggerated octahedral tilts ($143\text{-}146^\circ$) can be seen close to the interface with Nb:STO. In the inset of b, apart from marking selected oxygen column positions (red dotted circles), and Mn displacements from the center of an octahedron (green arrows), we also point out to some of the resolvable double oxygen columns between Mn columns (blue arrows). This is another feature of transformation towards square pyramidal coordination of Mn, as illustrated from the schematic of BM $\text{SrMnO}_{2.5}$ (SMO) in (C). (D) iDPC-STEM images from other regions (also in BM-precursor phase), where also Mn displacements (green arrows), and resolvable separation between oxygen columns between Mn columns (blue arrows) are marked. Scale bars, 1 nm in (A,B), 500 pm in (D) and inset (right panel) of B.

Fig. S3



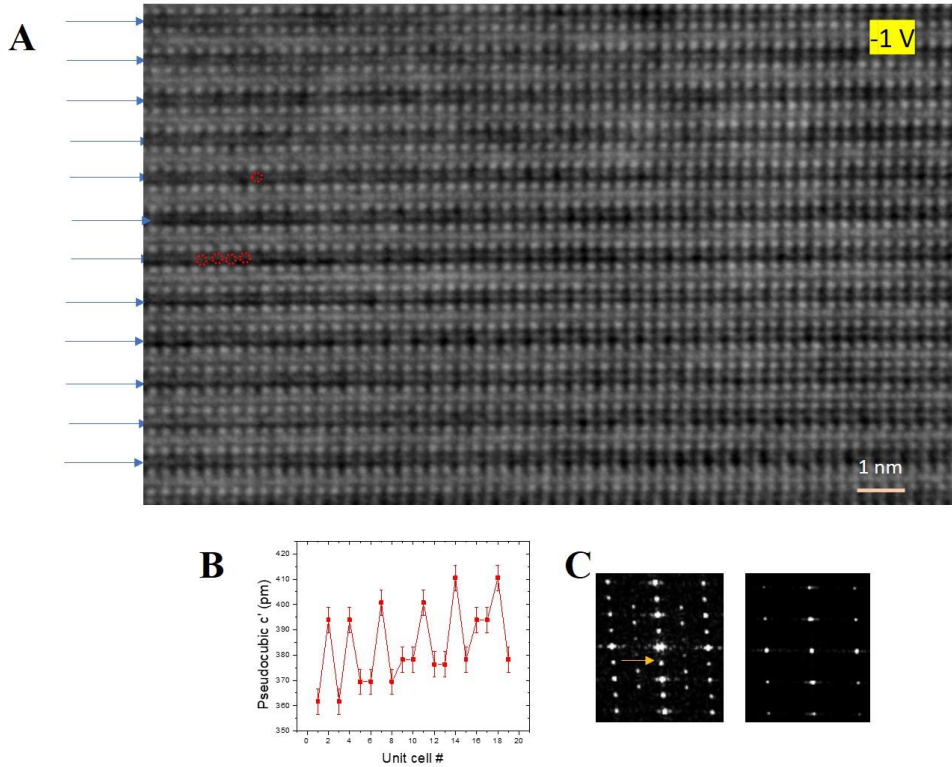
Statistical characterization of Mn displacements in BM precursor phase and virgin state (A) IDPC-STEM image of the LSMO layer in an LSMO/HZO/LSMO/Nb:STO device prior to the application of a bias voltage, with Mn displacements away from the center of the octahedron marked as arrows. (B) IDPC-STEM images of two representative regions in the LSMO layer of the same device with the Mn displacements away from the center of the octahedron marked as arrows. Note the larger random displacements compared to (A). (C) Polar scatter plot of Mn displacement vectors on a 60 pm radius circle for the virgin state (left, obtained from 60 Mn atomic columns) and the 2V biased state (right, obtained from 329 Mn atomic columns).

Fig. S4



Hysteretic BM phase: (A) HAADF-STEM and corresponding iDPC-STEM images of BM phase formed at 4 V. This is a domain whose c -axis is parallel to the viewing direction (zone axis). Schematic of this domain is also shown on the right most panel (La/Sr: green, Mn: red, O: brown). By comparing HAADF and iDPC-STEM images, it can be clearly noted that the first 2-3 monolayers of LSMO near the interface with the substrate are still in a BM-precursor phase. (B) HAADF-STEM and corresponding iDPC-STEM images of BM phase hystetically retained at 0 V. In the field of view, two domains of the BM phase can be noted (beyond the first 3 monolayers of LSMO near the substrate). They have a and c as the zone axes respectively. The back-to-back tetrahedra in alternate Mn-O planes along $[1-10]$ direction can be clearly observed from the domain viewed along a -axis (schematic in the right panel).

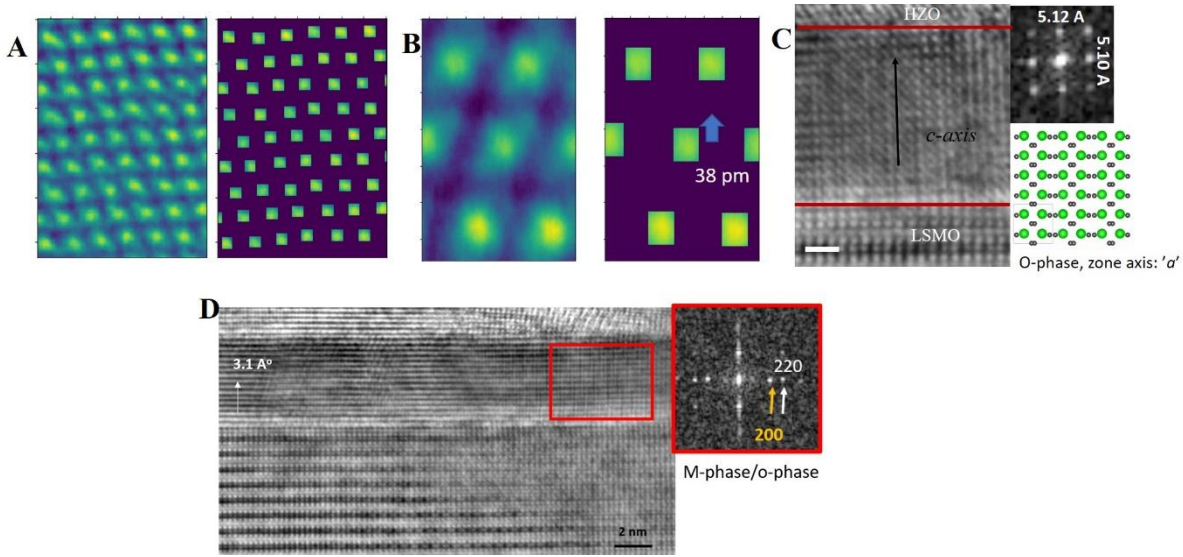
Fig S5



Reoxygenation of LSMO at negative bias and dynamics

(A) This iDPC-STEM image is obtained from a representative region in LSMO which has initially transformed to a BM phase upon poling at 4 V. Then, by applying -1 V, we clearly see oxygen columns appearing (some of them marked by red circles as a guide to eye) in the Mn-O planes in darker contrast (marked by blue arrows on the left). The appearance of these new positions also marks a transformation of this Mn-O layer with Mn in tetrahedral coordination to a Mn in higher coordination. (B) c' parameter oscillation across 20 unit cells of LSMO corresponding to Fig. 2C (poled at -3 V), reminiscent of the BM precursor phase. (C) Evolution of BM phase to perovskite phase within 90 seconds of changing the voltage from -3 V to +3 V, followed through Fast Fourier Transforms (for images presented in Fig. 2E). Notice the disappearance of the superstructure reflections upon this transformation.

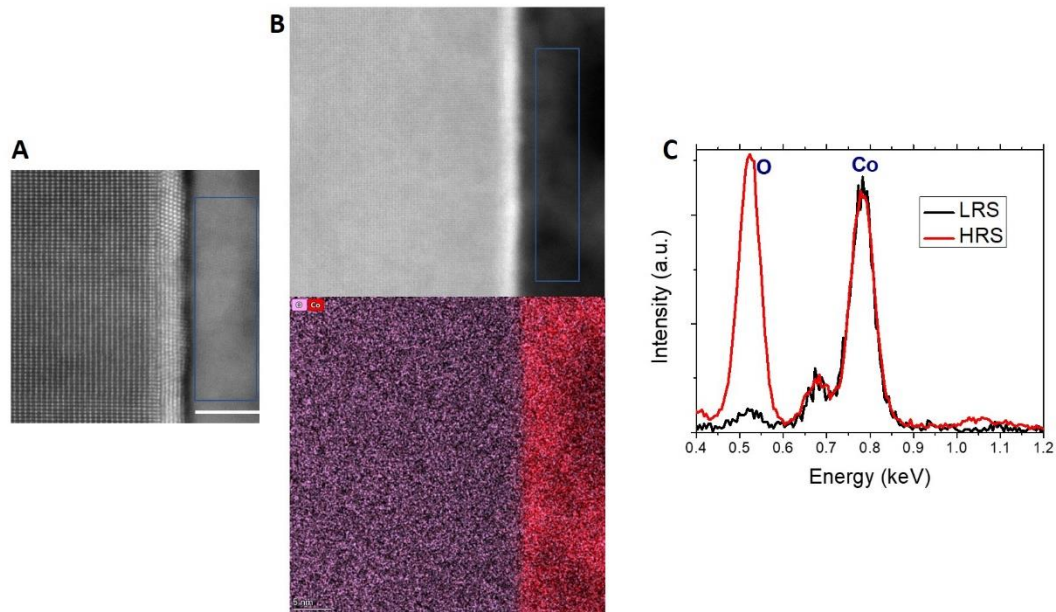
Fig. S6



Evolution of HZO layer

(A) The iDPC-STEM image of supercell of HZO r-phase grain presented in Fig. 3A at 1 V (left). Cationic lattice is shown on the right. The rest (difference image) is the anionic lattice. Difference in the CoM of cationic and anionic lattice reveals the \vec{V}_o displacement as a function of bias (Fig. 3B). (B) $R3m$ unit cell (iDPC-STEM image of the left domain in Fig. 3E) considered for direct P_r estimations. Upon symmetrizing this unit cell, $P_r=0$ in the paraelectric phase, and this justifies the selection of the unit cell. CoM cation–CoM non cationic part gives the displacement (38 pm in the unit cell shown here). This procedure includes the presence of \vec{V}_o , information present in the raw image contrast. (C) iDPC-STEM image of an o-phase with c-axis out-of-plane, observed at 4 V. FFT and the matching of experimental image to the real space schematic with Hf/Zr columns in green, and oxygen in grey confirm an o-phase. (D) Representative large field of view image of the LSMO/HZO/LSMO capacitor imaged after switching twice (switching cycle ends in 3V). Multigrained nature of HZO (either in m or o-phases) can be easily identified from FFT of the indicated region on the right side of the image. In the grain on the left side of the image, the c-parameter (3.1 \AA°) corresponds to the m-phase. Thus the r to o/m phase transition (and single grain to multigrainedness) is a reversible process in these experiments.

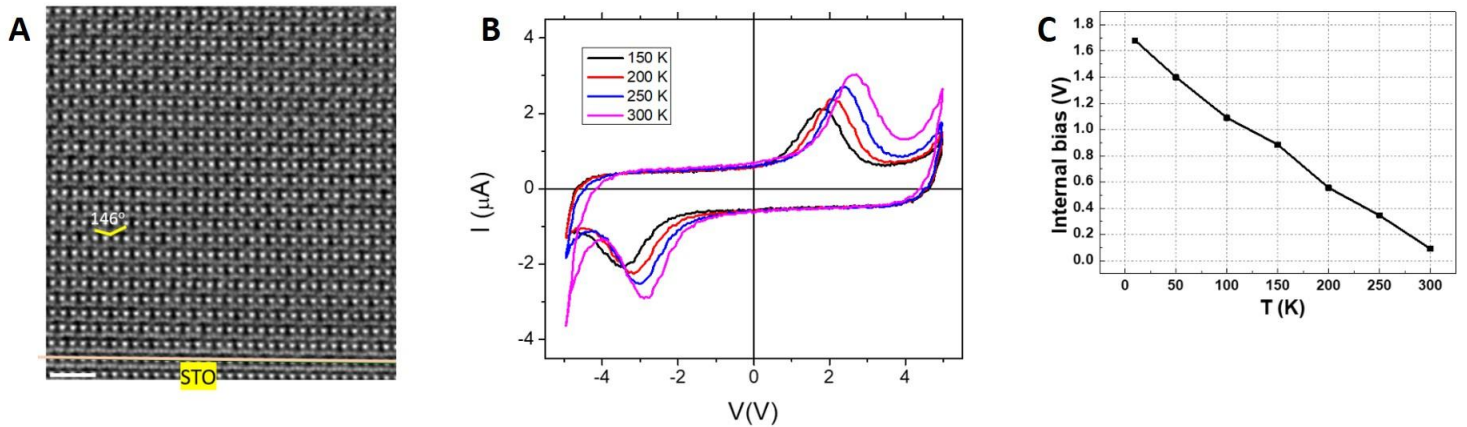
Fig. S7



Chemical analysis of cycled tunnel junctions

A) Tunnel junction device in LRS from which EDS spectrum is obtained from the Co electrode region shown in blue box. B) Tunnel junction device (top) in HRS from which EDS spectrum is collected. (down) EDS map of Co and O, clearly showing Co rich and CoO_x rich regions in the top electrode. Scale bar, 5 nm for both (A) and (B). (C) EDS integrated spectra (normalized to Co L-edge), obtained from the blue boxed regions shown in (A) and (B). The HRS clearly has a large oxygen content and LRS has almost negligible content.

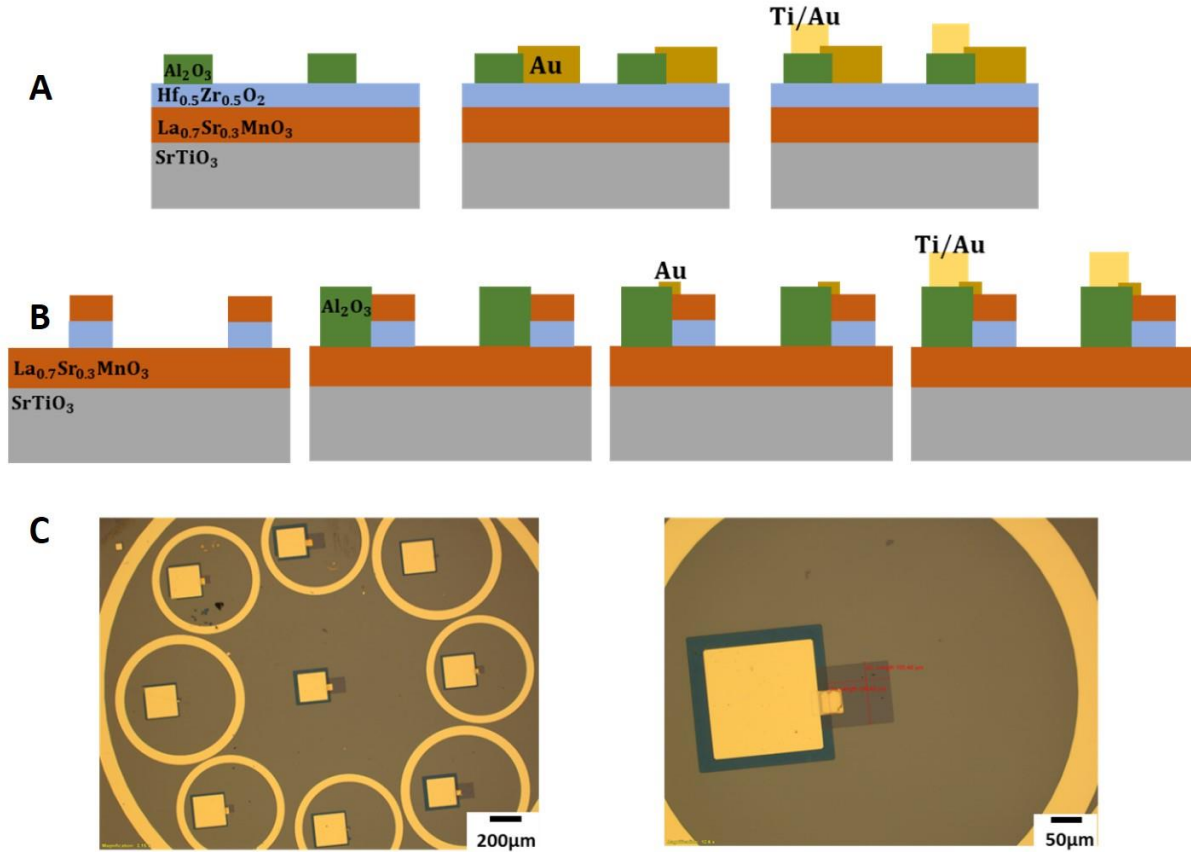
Fig. S8



TiN/HZO/LSMO capacitors with temperature

(A) IDPC-STEM image of LSMO layer close to STO interface in the “down” polarized state of the TiN/HZO/LSMO device shown in Fig 4D and E of the manuscript. Note the exaggerated octahedral tilts. (B) I-V loops corresponding to the P-V loops presented in Fig. 4C of the manuscript. The $2P_r$ increases with increasing temperature, as shown in the inset of Fig. 4C. (C) Internal bias, calculated as $V_{c+}+V_{c-}$ as a function of temperature, where V_{c+} (V_{c-}) are coercive voltages under positive (negative) bias.

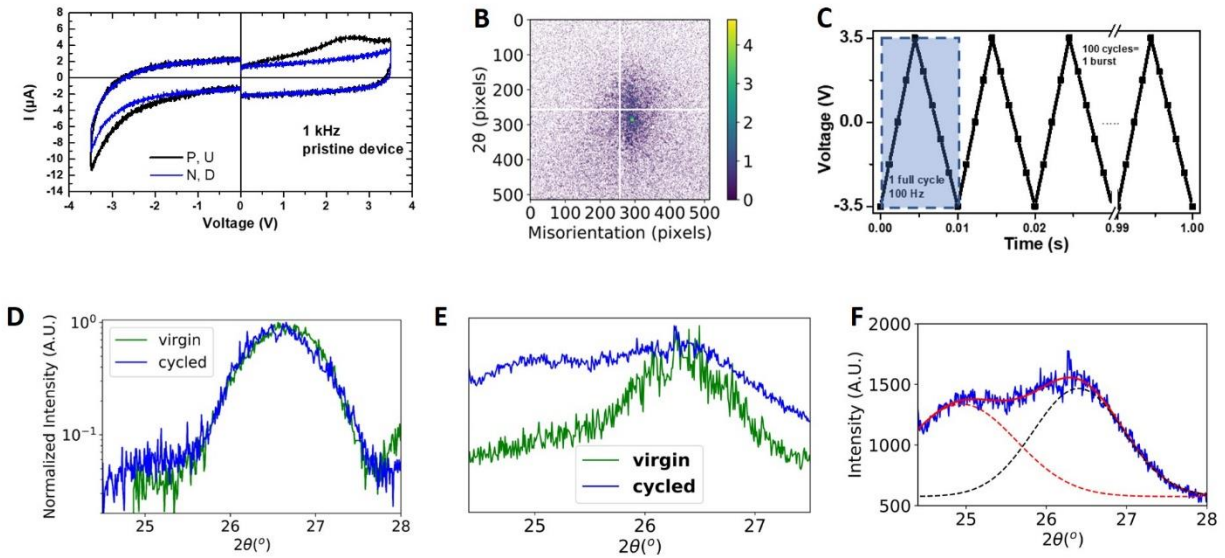
Fig. S9



Device fabrication for the operando nanobeam synchrotron diffraction experiment:

(A) and (B) show the device fabrication process flow diagrams for the Au/HZO/LSMO and LSMO/HZO/LSMO capacitors, respectively. Standard photolithography techniques and e-beam evaporation were used. For the LSMO/HZO/LSMO devices etching was initially performed for the removal of top LSMO and HZO layers in order to pattern the devices of interest. Subsequently, for both type of capacitors, a thick layer of Al_2O_3 is used as the insulating base for a thick Ti/Au wire-bonding pad. The top electrodes (Au in (A) and LSMO in (B)) were electrically connected with the wire-bonding pad through partial overlapping in (A) and through the deposition of Au connecting layers in (B). The design of these devices preserves the electrical connectivity of the capacitors while their top surface remains optically free to be probed with the X-ray nanobeam. In (C), optical microscope images show the final shape of the LSMO/HZO/LSMO. Au rings were used during the alignment of the nanobeam.

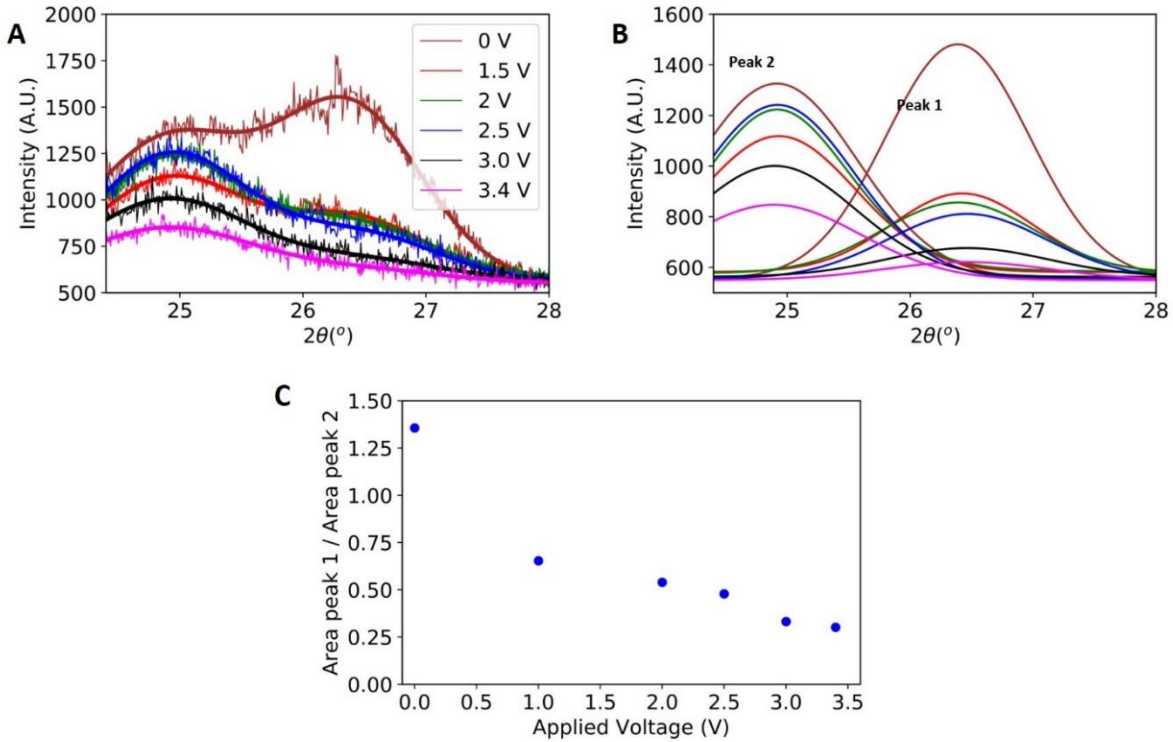
Fig S10



Operando nanobeam synchrotron diffraction results on Au/HZO/LSMO capacitors

A) I-V plots obtained from a PUND measurement on the Au/HZO/LSMO device tested in the Nanomax beamline (Max IV synchrotron, Lund, Sweden). B) Detector image at the Bragg peak position of HZO showing intense specular signal, and diffuse non-sepcular signal. C) 100 Hz biasing scheme used for the *operando* XRD measurements (the dots represent the 1 kHz measurement scheme used for dynamical measurements during cycling, not shown here). LSMO/HZO/LSMO and Au/HZO/LSMO capacitors were cycled for tens of thousands of times. D) 2θ projections of the 2D data obtained on LSMO/HZO/LSMO device before cycling (green) and after cycling showing no obvious changes. E) 2θ projection of the 2D data obtained on Au/HZO/LSMO device before cycling (green) and after cycling showing the appearance of a distinct peak related to a monoclinic phase with cycling. (F) Pseudo-voigt fits to data on cycled devices shown in (E).

Fig. S11



Phase analysis in HZO layer with positive DC bias in Au/HZO/LSMO capacitors:

2θ projections with DC bias on cycled Au/HZO/LSMO capacitor devices (A), the pseudo-Voigt fits of r-phase (right) and m-phase peaks (left) (B), and comparison of r/m peak intensities as a function of applied bias (C).

References and Notes

1. T. S. Böscke, J. Müller, D. Bräuhaus, U. Schröder, U. Böttger, Ferroelectricity in hafnium oxide thin films. *Appl. Phys. Lett.* **99**, 102903 (2011). [doi:10.1063/1.3634052](https://doi.org/10.1063/1.3634052)
2. A. Chernikova, M. Kozodaev, A. Markeev, D. Negrov, M. Spiridonov, S. Zarubin, O. Bak, P. Buragohain, H. Lu, E. Suvorova, A. Gruverman, A. Zenkevich, Ultrathin Hf_{0.5}Zr_{0.5}O₂ Ferroelectric Films on Si. *ACS Appl. Mater. Interfaces* **8**, 7232–7237 (2016). [doi:10.1021/acsami.5b11653](https://doi.org/10.1021/acsami.5b11653) [Medline](#)
3. X. Tian, S. Shibayama, T. Nishimura, T. Yajima, S. Migita, A. Toriumi, Evolution of ferroelectric HfO₂ in ultrathin region down to 3 nm. *Appl. Phys. Lett.* **112**, 102902 (2018). [doi:10.1063/1.5017094](https://doi.org/10.1063/1.5017094)
4. S. S. Cheema, D. Kwon, N. Shanker, R. Dos Reis, S.-L. Hsu, J. Xiao, H. Zhang, R. Wagner, A. Datar, M. R. McCarter, C. R. Serrao, A. K. Yadav, G. Karbasian, C.-H. Hsu, A. J. Tan, L.-C. Wang, V. Thakare, X. Zhang, A. Mehta, E. Karapetrova, R. V. Chopdekar, P. Shafer, E. Arenholz, C. Hu, R. Proksch, R. Ramesh, J. Ciston, S. Salahuddin, Enhanced ferroelectricity in ultrathin films grown directly on silicon. *Nature* **580**, 478–482 (2020). [doi:10.1038/s41586-020-2208-x](https://doi.org/10.1038/s41586-020-2208-x) [Medline](#)
5. U. Schröder, C. S. Hwang, H. Funakubo, Eds., *Ferroelectricity in Doped Hafnium Oxide* (Woodhead Publishing, ed. 1, 2019).
6. P. Nukala, Y. Wei, V. de Haas, Q. Guo, J. Antoja-Lleonart, B. Noheda, Guidelines for the stabilization of a polar rhombohedral phase in epitaxial Hf_{0.5}Zr_{0.5}O₂ thin films. *Ferroelectrics* **569**, 148–163 (2020). [doi:10.1080/00150193.2020.1791658](https://doi.org/10.1080/00150193.2020.1791658)
7. Y. Wei, P. Nukala, M. Salverda, S. Matzen, H. J. Zhao, J. Momand, A. S. Everhardt, G. Agnus, G. R. Blake, P. Lecoeur, B. J. Kooi, J. Íñiguez, B. Dkhil, B. Noheda, A rhombohedral ferroelectric phase in epitaxially strained Hf_{0.5}Zr_{0.5}O₂ thin films. *Nat. Mater.* **17**, 1095–1100 (2018). [doi:10.1038/s41563-018-0196-0](https://doi.org/10.1038/s41563-018-0196-0) [Medline](#)
8. R. Materlik, C. Kunneth, A. Kersch, The origin of ferroelectricity in Hf_{1-x}Zr_xO₂: A computational investigation and a surface energy model. *J. Appl. Phys.* **117**, 134109 (2015). [doi:10.1063/1.4916707](https://doi.org/10.1063/1.4916707)
9. S. J. Kim, J. Mohan, S. R. Summerfelt, J. Kim, Ferroelectric Hf_{0.5}Zr_{0.5}O₂ Thin Films: A Review of Recent Advances. *JOM* **71**, 246–255 (2019). [doi:10.1007/s11837-018-3140-5](https://doi.org/10.1007/s11837-018-3140-5)
10. T. Mimura, T. Shimizu, H. Funakubo, Ferroelectricity in YO_{1.5}-HfO₂ films around 1 μm in thickness. *Appl. Phys. Lett.* **115**, 032901 (2019). [doi:10.1063/1.5097880](https://doi.org/10.1063/1.5097880)
11. X. Xu, F.-T. Huang, Y. Qi, S. Singh, K. M. Rabe, D. Obeysekera, J. Yang, M.-W. Chu, S.-W. Cheong, Kinetically stabilized ferroelectricity in bulk single-crystalline HfO₂:Y. *Nat. Mater.* [10.1038/s41563-020-00897-x](https://doi.org/10.1038/s41563-020-00897-x) (2021). [doi:10.1038/s41563-020-00897-x](https://doi.org/10.1038/s41563-020-00897-x) [Medline](#)
12. Y. Zhou, Y. K. Zhang, Q. Yang, J. Jiang, P. Fan, M. Liao, Y. C. Zhou, The effects of oxygen vacancies on ferroelectric phase transition of HfO₂-based thin film from first-principle. *Comput. Mater. Sci.* **167**, 143–150 (2019). [doi:10.1016/j.commatsci.2019.05.041](https://doi.org/10.1016/j.commatsci.2019.05.041)
13. H. Mulaosmanovic, J. Ocker, S. Müller, U. Schroeder, J. Müller, P. Polakowski, S. Flachowsky, R. van Bentum, T. Mikolajick, S. Slesazeck, Switching kinetics in nanoscale

- hafnium oxide based ferroelectric field-effect transistors. *ACS Appl. Mater. Interfaces* **9**, 3792–3798 (2017). [doi:10.1021/acsami.6b13866](https://doi.org/10.1021/acsami.6b13866) [Medline](#)
14. M. Pešić, C. Künneth, M. Hoffmann, H. Mulaosmanovic, S. Müller, E. T. Breyer, U. Schroeder, A. Kersch, T. Mikolajick, S. Slesazeck, A computational study of hafnia-based ferroelectric memories: From ab initio via physical modeling to circuit models of ferroelectric device. *J. Comput. Electron.* **16**, 1236–1256 (2017). [doi:10.1007/s10825-017-1053-0](https://doi.org/10.1007/s10825-017-1053-0)
 15. N. Gong, X. Sun, H. Jiang, K. S. Chang-Liao, Q. Xia, T. P. Ma, Nucleation limited switching (NLS) model for HfO₂-based metal-ferroelectric-metal (MFM) capacitors: Switching kinetics and retention characteristics. *Appl. Phys. Lett.* **112**, 262903 (2018). [doi:10.1063/1.5010207](https://doi.org/10.1063/1.5010207)
 16. P. Buragohain, C. Richter, T. Schenk, H. Lu, T. Mikolajick, U. Schroeder, A. Gruverman, Nanoscopic studies of domain structure dynamics in ferroelectric La:HfO₂ capacitors. *Appl. Phys. Lett.* **112**, 222901 (2018). [doi:10.1063/1.5030562](https://doi.org/10.1063/1.5030562)
 17. S. Migita, H. Ota, H. Yamada, K. Shibuya, A. Sawa, A. Toriumi, Polarization switching behavior of Hf-Zr-O ferroelectric ultrathin films studied through coercive field characteristics. *Jpn. J. Appl. Phys.* **57**, 04FB01 (2018). [doi:10.7567/JJAP.57.04FB01](https://doi.org/10.7567/JJAP.57.04FB01)
 18. Y. H. Lee, S. D. Hyun, H. J. Kim, J. S. Kim, C. Yoo, T. Moon, K. D. Kim, H. W. Park, Y. B. Lee, B. S. Kim, J. Roh, M. H. Park, C. S. Hwang, Nucleation-Limited Ferroelectric Orthorhombic Phase Formation in Hf_{0.5}Zr_{0.5}O₂ Thin Films. *Adv. Electron. Mater.* **5**, 180436 (2019). [doi:10.1002/aelm.201800436](https://doi.org/10.1002/aelm.201800436)
 19. T. Schenk, M. Hoffmann, J. Ocker, M. Pešić, T. Mikolajick, U. Schroeder, Complex internal bias fields in ferroelectric hafnium oxide. *ACS Appl. Mater. Interfaces* **7**, 20224–20233 (2015). [doi:10.1021/acsami.5b05773](https://doi.org/10.1021/acsami.5b05773) [Medline](#)
 20. H.-J. Lee, M. Lee, K. Lee, J. Jo, H. Yang, Y. Kim, S. C. Chae, U. Waghmare, J. H. Lee, Scale-free ferroelectricity induced by flat phonon bands in HfO₂. *Science* **369**, 1343–1347 (2020). [doi:10.1126/science.aba0067](https://doi.org/10.1126/science.aba0067) [Medline](#)
 21. C. Li, Y. Yao, X. Shen, Y. Wang, J. Li, C. Gu, R. Yu, Q. Liu, M. Liu, Dynamic observation of oxygen vacancies in hafnia layer by *in situ* transmission electron microscopy. *Nano Res.* **8**, 3571–3579 (2015). [doi:10.1007/s12274-015-0857-0](https://doi.org/10.1007/s12274-015-0857-0)
 22. S. U. Sharath, S. Vogel, L. Molina-Luna, E. Hildebrandt, C. Wenger, J. Kurian, M. Duerrschnabel, T. Niermann, G. Niu, P. Calka, M. Lehmann, H. J. Kleebe, T. Schroeder, L. Alff, Control of Switching Modes and Conductance Quantization in Oxygen Engineered HfO_x based Memristive Devices. *Adv. Funct. Mater.* **27**, 1700432 (2017). [doi:10.1002/adfm.201700432](https://doi.org/10.1002/adfm.201700432)
 23. Y. Wei, S. Matzen, C. P. Quinteros, T. Maroutian, G. Agnus, P. Lecoeur, B. Noheda, Magneto-ionic control of spin polarization in multiferroic tunnel junctions. *npj Quantum Mater.* **4**, 62 (2019). [doi:10.1038/s41535-019-0201-0](https://doi.org/10.1038/s41535-019-0201-0)
 24. M. C. Sulzbach, S. Estandía, X. Long, J. Lyu, N. Dix, J. Gàzquez, M. F. Chisholm, F. Sánchez, I. Fina, J. Fontcuberta, Unraveling Ferroelectric Polarization and Ionic Contributions to Electroresistance in Epitaxial Hf_{0.5}Zr_{0.5}O₂ Tunnel Junctions. *Adv. Electron. Mater.* **6**, 1900852 (2020). [doi:10.1002/aelm.201900852](https://doi.org/10.1002/aelm.201900852)

25. M. Hambe, A. Petraru, N. A. Pertsev, P. Munroe, V. Nagarajan, H. Kohlstedt, Crossing an interface: Ferroelectric control of tunnel currents in magnetic complex oxide heterostructures. *Adv. Funct. Mater.* **20**, 2436–2441 (2010). [doi:10.1002/adfm.201000265](https://doi.org/10.1002/adfm.201000265)
26. D. Pantel, S. Goetze, D. Hesse, M. Alexe, Room-temperature ferroelectric resistive switching in ultrathin $\text{Pb}(\text{Zr}_{0.2}\text{Ti}_{0.8})\text{O}_3$ films. *ACS Nano* **5**, 6032–6038 (2011). [doi:10.1021/nm2018528](https://doi.org/10.1021/nm2018528) [Medline](#)
27. S. Boyn, J. Grollier, G. Lecerf, B. Xu, N. Locatelli, S. Fusil, S. Girod, C. Carrétéro, K. Garcia, S. Xavier, J. Tomas, L. Bellaiche, M. Bibes, A. Barthélémy, S. Saïghi, V. Garcia, Learning through ferroelectric domain dynamics in solid-state synapses. *Nat. Commun.* **8**, 14736 (2017). [doi:10.1038/ncomms14736](https://doi.org/10.1038/ncomms14736) [Medline](#)
28. V. Rouco, R. E. Hage, A. Sander, J. Grandal, K. Seurre, X. Palermo, J. Briatico, S. Collin, J. Trastoy, K. Bouzehouane, A. I. Buzdin, G. Singh, N. Bergeal, C. Feuillet-Palma, J. Lesueur, C. Leon, M. Varela, J. Santamaría, J. E. Villegas, Quasiparticle tunnel electroresistance in superconducting junctions. *Nat. Commun.* **11**, 658 (2020). [doi:10.1038/s41467-020-14379-w](https://doi.org/10.1038/s41467-020-14379-w) [Medline](#)
29. V. Mikheev, A. Choupruk, Y. Lebedinskii, S. Zarubin, Y. Matveyev, E. Kondratyuk, M. G. Kozodaev, A. M. Markeev, A. Zenkevich, D. Negrov, Ferroelectric Second-Order Memristor. *ACS Appl. Mater. Interfaces* **11**, 32108–32114 (2019). [doi:10.1021/acsami.9b08189](https://doi.org/10.1021/acsami.9b08189) [Medline](#)
30. M. D. Glinchuk, A. N. Morozovska, A. Lukowiak, W. Stręk, M. V. Silibin, D. V. Karpinsky, Y. Kim, S. V. Kalinin, Possible electrochemical origin of ferroelectricity in HfO_2 thin films. *J. Alloys Compd.* **830**, 153628 (2020). [doi:10.1016/j.jallcom.2019.153628](https://doi.org/10.1016/j.jallcom.2019.153628)
31. M. Qian, I. Fina, M. C. Sulzbach, F. Sánchez, J. Fontcuberta, Synergetic Electronic and Ionic Contributions to Electroresistance in Ferroelectric Capacitors. *Adv. Electron. Mater.* **5**, 1800646 (2019). [doi:10.1002/aelm.201800646](https://doi.org/10.1002/aelm.201800646)
32. C. Ferreyra, M. Rengifo, M. J. Sánchez, A. S. Everhardt, B. Noheda, D. Rubi, Key Role of Oxygen-Vacancy Electromigration in the Memristive Response of Ferroelectric Devices. *Phys. Rev. Appl.* **14**, 044045 (2020). [doi:10.1103/PhysRevApplied.14.044045](https://doi.org/10.1103/PhysRevApplied.14.044045)
33. M. Pešić, F. P. G. Fengler, L. Larcher, A. Padovani, T. Schenk, E. D. Grimley, X. Sang, J. M. LeBeau, S. Slesazeck, U. Schroeder, T. Mikolajick, Physical Mechanisms behind the Field-Cycling Behavior of HfO_2 -Based Ferroelectric Capacitors. *Adv. Funct. Mater.* **26**, 4601–4612 (2016). [doi:10.1002/adfm.201600590](https://doi.org/10.1002/adfm.201600590)
34. P. Gao, C. T. Nelson, J. R. Jokisaari, S. H. Baek, C. W. Bark, Y. Zhang, E. Wang, D. G. Schlom, C. B. Eom, X. Pan, Revealing the role of defects in ferroelectric switching with atomic resolution. *Nat. Commun.* **2**, 591 (2011). [doi:10.1038/ncomms1600](https://doi.org/10.1038/ncomms1600) [Medline](#)
35. Materials and methods are available as supplementary materials online.
36. S. de Graaf, J. Momand, C. Mitterbauer, S. Lazar, B. J. Kooi, Resolving hydrogen atoms at metal-metal hydride interfaces. *Sci. Adv.* **6**, eaay4312 (2020). [doi:10.1126/sciadv.aay4312](https://doi.org/10.1126/sciadv.aay4312) [Medline](#)

37. G. Sanchez-Santolino, M. Cabero, M. Varela, J. Garcia-Barriocanal, C. Leon, S. J. Pennycook, J. Santamaria, Oxygen octahedral distortions in LaMO₃/SrTiO₃ superlattices. *Microsc. Microanal.* **20**, 825–831 (2014). [doi:10.1017/S1431927614000750](https://doi.org/10.1017/S1431927614000750) [Medline](#)
38. S. Stølen, E. Bakken, C. E. Mohn, Oxygen-deficient perovskites: Linking structure, energetics and ion transport. *Phys. Chem. Chem. Phys.* **8**, 429–447 (2006). [doi:10.1039/B512271F](https://doi.org/10.1039/B512271F) [Medline](#)
39. P. Nukala, M. Ahmadi, J. Antoja-Lleonart, S. de Graaf, Y. Wei, H. W. Zandbergen, B. J. Kooi, B. Noheda, *In situ* heating studies on temperature-induced phase transitions in epitaxial Hf_{0.5}Zr_{0.5}O₂/La_{0.67}Sr_{0.33}MnO₃ heterostructures. *Appl. Phys. Lett.* **118**, 062901 (2021). [doi:10.1063/5.0035714](https://doi.org/10.1063/5.0035714)
40. L. Cao, O. Petravic, P. Zakalek, A. Weber, U. Rücker, J. Schubert, A. Koutsioubas, S. Mattauch, T. Brückel, Reversible Control of Physical Properties via an Oxygen-Vacancy-Driven Topotactic Transition in Epitaxial La_{0.7}Sr_{0.3}MnO_{3-δ} Thin Films. *Adv. Mater.* **31**, 1806183 (2019). [doi:10.1002/adma.201806183](https://doi.org/10.1002/adma.201806183)
41. L. Yao, S. Inkinen, S. van Dijken, Direct observation of oxygen vacancy-driven structural and resistive phase transitions in La_{2/3}Sr_{1/3}MnO₃. *Nat. Commun.* **8**, 14544 (2017). [doi:10.1038/ncomms14544](https://doi.org/10.1038/ncomms14544) [Medline](#)
42. C. Baeumer, C. Schmitz, A. H. H. Ramadan, H. Du, K. Skaja, V. Feyer, P. Müller, B. Arndt, C. L. Jia, J. Mayer, R. A. De Souza, C. Michael Schneider, R. Waser, R. Dittmann, Spectromicroscopic insights for rational design of redox-based memristive devices. *Nat. Commun.* **6**, 8610 (2015). [doi:10.1038/ncomms9610](https://doi.org/10.1038/ncomms9610) [Medline](#)
43. L. Bégon-Lours, M. Mulder, P. Nukala, S. De Graaf, Y. A. Birkhölzer, B. Kooi, B. Noheda, G. Koster, G. Rijnders, Stabilization of phase-pure rhombohedral HfZrO₄ in pulsed laser deposited thin films. *Phys. Rev. Mater.* **4**, 043401 (2020). [doi:10.1103/PhysRevMaterials.4.043401](https://doi.org/10.1103/PhysRevMaterials.4.043401)
44. Y. Wei, S. Matzen, T. Maroutian, G. Agnus, M. Salverda, P. Nukala, Q. Chen, J. Ye, P. Lecoeur, B. Noheda, Magnetic Tunnel Junctions Based on Ferroelectric Hf_{0.5}Zr_{0.5}O₂ Tunnel Barriers. *Phys. Rev. Appl.* **12**, 031001 (2019). [doi:10.1103/PhysRevApplied.12.031001](https://doi.org/10.1103/PhysRevApplied.12.031001)
45. W. Hamouda, C. Lubin, S. Ueda, Y. Yamashita, O. Renault, F. Mehmood, T. Mikolajick, U. Schroeder, R. Negrea, N. Barrett, Interface chemistry of pristine TiN/La: Hf_{0.5}Zr_{0.5}O₂ capacitors. *Appl. Phys. Lett.* **116**, 252903 (2020). [doi:10.1063/5.0012595](https://doi.org/10.1063/5.0012595)
46. S. Santucci, H. Zhang, S. Sanna, N. Pyrds, V. Esposito, Electro-chemo-mechanical effect in Gd-doped ceria thin films with a controlled orientation. *J. Mater. Chem. A* **8**, 14023–14030 (2020). [doi:10.1039/D0TA05500J](https://doi.org/10.1039/D0TA05500J)
47. A. Herpers, C. Lenser, C. Park, F. Offi, F. Borgatti, G. Panaccione, S. Menzel, R. Waser, R. Dittmann, Spectroscopic proof of the correlation between redox-state and charge-carrier transport at the interface of resistively switching Ti/PCMO devices. *Adv. Mater.* **26**, 2730–2735 (2014). [doi:10.1002/adma.201304054](https://doi.org/10.1002/adma.201304054) [Medline](#)
48. G. Radaelli, D. Gutiérrez, F. Sánchez, R. Bertacco, M. Stengel, J. Fontcuberta, Large room-temperature electroresistance in dual-modulated ferroelectric tunnel barriers. *Adv. Mater.* **27**, 2602–2607 (2015). [doi:10.1002/adma.201405117](https://doi.org/10.1002/adma.201405117) [Medline](#)

49. P. Nukala, M. Ahmadi, Y. Wei, S. de Graaf, E. Stylianidis, T. Chakraborty, S. Matzen, H. W. Zandbergen, A. Björling, D. Mannix, D. Carbone, B. Kooi, B. Noheda, Dataset: Reversible oxygen migration and phase transitions in hafnia-based ferroelectric devices, version 1.0, Dataverse NL (2021); <https://doi.org/10.34894/EIOXPT>.
50. U. Johansson, U. Voigt, A. Mikkelsen, NanoMAX: A hard x-ray beamline at MAX IV, *Proc. SPIE* **8851**, 88510L (2013). [doi:10.1117/12.2026609](https://doi.org/10.1117/12.2026609)
51. A. Björling, S. Kalbfleisch, M. Kahnt, S. Sala, K. Parfeniukas, U. Vogt, D. Carbone, U. Johansson, Ptychographic characterization of a coherent nanofocused X-ray beam. *Opt. Express* **28**, 5069–5076 (2020). [doi:10.1364/OE.386068](https://doi.org/10.1364/OE.386068) [Medline](#)
52. Z. Horita, T. Sano, M. Nemoto, Energydispersive x-ray microanalysis in the analytical electron microscope. *ISIJ Int.* **29**, 179–190 (1989). [doi:10.2355/isijinternational.29.179](https://doi.org/10.2355/isijinternational.29.179)
53. F. P. G. Fengler, M. Pešić, S. Starschich, T. Schneller, C. Künneth, U. Böttger, H. Mulaosmanovic, T. Schenk, M. H. Park, R. Nigon, P. Mural, T. Mikolajick, U. Schroeder, Domain Pinning: Comparison of Hafnia and PZT Based Ferroelectrics. *Adv. Electron. Mater.* **3**, 1600505 (2017). [doi:10.1002/aelm.201600505](https://doi.org/10.1002/aelm.201600505)